Article

Angle-Independent Surface-Instability Hydrogel Sensors Enabled by Thickness Control

Ruoyi Ke †, Imri Frenkel †, Zixiao Liu, Chuan Wei Zhang, Ping He, Pengju Shi, Abdullatif Jazzar, Yousif Alsaid, Yingjie Du, Sidi Duan, Dong Wu, Mutian Hua, Shuwang Wu, and Ximin He *

Department of Materials Science and Engineering, University of California, Los Angeles, CA 90095, USA
* Correspondence: ximinhe@ucla.edu
† These authors contributed equally to this work.
Received: 9 July 2025; Revised: 26 August 2025; Accepted: 1 September 2025; Published: 4 September 2025

Abstract: Surface instability-based hydrogel sensors offer equipment-free visual detection but suffer from severe angle-dependent visibility that limits practical applications. Here we demonstrate that film thickness serves as a critical fourth design parameter—beyond elastic modulus, swelling ratio, and stimulus concentration—to achieve omnidirectional optical readout. Through systematic optimization across poly(2-(dimethylamino) ethyl methacrylate) (PDMAEMA), poly(acrylamide-co-acrylic acid) (P(AAm-*co*-AAc)), and poly(N-isopropylacrylamide-co-acrylamide) (P(NIPAm-*co*-Am)) systems, we identify an operational thickness window of 160–1300 μm, with 300 μm producing wrinkle dimensions that match visible light wavelengths for angle-independent scattering. This morphological control reduces viewing angle effects by >80%, enabling reliable naked-eye detection across a wide viewing angle range (0–60°), representing an >80% improvement over previous angle-dependent sensors. We validate this design framework through enzyme-coupled glucose sensors operating across clinical ranges (200–1000 mg/dL) and direct polarity sensors with binary discrimination at Polarity Index (PI) ~3.5. Exploiting the threshold nature of instability-induced scattering (IIS), we further demonstrate soft material logic gates (AND, OR, XOR) that process environmental stimuli and autonomously control LCE actuators within 15 s—establishing the examples of hydrogel-based Boolean computation without electronic components. These advances transform IIS sensors from laboratory curiosities into practical platforms for soft robotics and autonomous systems.

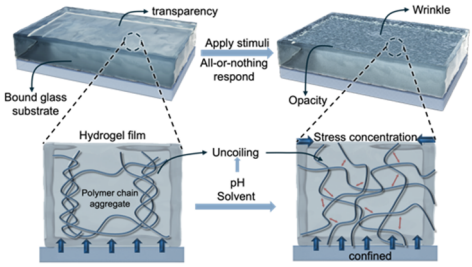

Keywords: hydrogel sensors; surface instability; angle-independent detection; material-based computation; soft robotics

1. Introduction

Intelligent responsive materials capable of sensing environmental changes and transducing them into measurable outputs have emerged as transformative alternatives to traditional rigid electronic sensors [1–4]. Among these, hydrogel-based smart sensors offer unprecedented advantages through their unique combination of high water content (up to 99%) [5], mechanical flexibility, and stimuli-responsive behavior [6,7], enabling seamless integration with biological systems while achieving molecular-level detection capabilities and maintaining mechanical compliance similar to soft tissues [8]. Unlike conventional electronic sensors that require complex fabrication processes, external power sources, and suffer from biocompatibility issues, hydrogel sensors leverage volume phase transitions (VPT) [9,10] to achieve detection sensitivities down to femtomolar concentrations [11] through simple swelling/deswelling mechanisms. Pioneering work on pH-responsive hydrogels has demonstrated remarkable volume changes, with poly(2-hydroxyethyl methacrylate) systems exhibiting swelling ratios from 40% to 80% under alkaline conditions [12], while temperature-responsive poly(N-isopropylacrylamide) systems show sharp transitions at physiologically relevant temperatures [13], and glucose-

sensing hydrogels incorporating enzymes enable continuous monitoring [14]. Notably, fiber-optic interferometric sensors incorporating responsive hydrogels have demonstrated detection limits down to nanomolar concentrations [15], with some systems achieving refractive index sensitivities surpassing 0.001 RIU resolution [16], representing orders of magnitude improvement over conventional methods by exploiting optical interference patterns in hydrogel matrices. Beyond sensing, these materials have enabled remarkable advances in soft robotics, with light-guided swimming robots achieving speeds up to 19.2 mm/s through photothermal Marangoni effects while incorporating multi-band electromagnetic stealth capabilities [17]. These developments have addressed fundamental challenges in the sensor field by combining the biocompatibility and flexibility of hydrogels with detection sensitivities that match or exceed traditional electronic sensors, paving the way for applications in wearable health monitoring [18], environmental sensing [19], and biomedical diagnostics [20] where rigid electronics would be impractical.

Among the diverse landscape of smart material sensors, self-reporting capability represent a critical advancement by fundamentally solving the instrumentation dependency [21] that has limited practical deployment of responsive hydrogels. Traditional hydrogel sensors, despite their excellent sensitivity and biocompatibility, typically require external equipment such as spectrophotometers, electrochemical analyzers, or mechanical testing apparatus to transduce and quantify their responses, adding cost, complexity, and limiting portability [22–24]. Self-reporting sensor address this challenge by integrating both sensing and signaling functions within a single material platform, producing visually observable outputs—such as color changes [25,26], fluorescence modulation [27,28], or transparency-to-opacity transitions [29]—that can be interpreted with the naked eye. Frenkel et al. [30] exemplified this approach by developing self-reporting hydrogel sensors based on surface IIS, establishing a three-parameter design space encompassing elastic modulus, critical swelling ratio, and stimulus concentration, where hydrogel films transition from transparent to opaque states upon reaching critical analyte concentrations. This capability is particularly transformative for point-of-care diagnostics, environmental monitoring in resource-limited settings, and wearable health devices where conventional readout equipment would be impractical or prohibitively expensive, demonstrating that sophisticated sensing can be achieved without any external power or readout devices.

However, when integrating self-reporting sensors into intelligent systems for autonomous decision-making and actuation, a critical challenge emerges: angle-dependent visibility that compromises reliable signal interpretation [31–33]. This limitation, inherent to many optical self-reporting mechanisms including surface instability-based sensors [34], arises from the wavelength-dependent light scattering of surface features that vary with observation angle—a well-documented phenomenon in rough surface optics where the angular dependence of scattered light intensity can vary significantly with viewing geometry [35]. Studies on rough surfaces have demonstrated that the intensity of scattered radiation generally decreases with increasing reflection angle [36], with some systems showing variations in optical response that can compromise measurement reliability when the observation angle deviates from normal incidence [37]. Such angle sensitivity severely restricts practical applications where consistent readout is essential, particularly in soft robotic systems [38,39], wearable devices [40], or automated monitoring platforms [41] where sensor orientation cannot be precisely controlled. Previous IIS sensors required oblique viewing angles to confirm wrinkled states, as surface instabilities were not discernibly opaque when observed head-on [30], fundamentally limiting their integration into autonomous systems that rely on unambiguous binary signals. We propose that systematic optimization of film thickness—a previously overlooked fourth design parameter—can fundamentally resolve this angle-dependency by tuning the characteristic wavelength of surface features to match visible light wavelengths, thereby achieving robust omnidirectional visibility essential for intelligent system integration.

Here, we present a comprehensive design strategy that advances IIS sensors from angle-dependent reporters to omnidirectional smart material computing elements suitable for autonomous soft robotic systems. By systematically investigating the role of film thickness across multiple stimuli-responsive polymer systems—including cationic PDMAEMA for pH sensing and P(NIPAm-*co*-Am) for solvent polarity detection—we establish that thickness optimization within the 160–1300 μm range enables angle-independent visibility through precise matching of wrinkle wavelengths with visible light. We demonstrate that this fourth design parameter not only resolves the fundamental optical limitations but also enables the construction of soft material logic gates (AND, OR, XOR) by exploiting the discrete threshold-dependent transitions inherent to IIS sensors. Furthermore, we integrate these logic elements with liquid crystal elastomer (LCE) actuators to create fully autonomous soft robotic systems capable of sensing environmental stimuli, processing information through material-based computation, and executing mechanical responses without any electronic components—achieving the first demonstration of closed-loop intelligent behavior in purely soft material systems. This work establishes a new paradigm where

materials themselves become autonomous agents capable of sophisticated decision-making, opening unprecedented possibilities for soft robotics, biomedical devices, and adaptive systems.

2. Experimental Methods

2.1. Chemicals and Materials

2-(dimethylamino)ethyl methacrylate (DMAEMA), acrylamide, acrylic acid, N-isopropyl acrylamide (NIPAm), N,N′-Methylenebisacrylamide (Bis), poly(ethylene glycol) diacrylate (PEGDA) (Mn = 250; 525; and 700), Lithium phenyl-2,4,6-trimethylbenzoylphosphinate (TPO-Li), 1-[4-(2-Hydroxyethoxy)-phenyl]-2-hydroxy-2-methyl-1-propane-1-one (Irgacure 2959), 2-hydroxy-2-methylpropiophenone (Darocur 1173), azobisisobutyronitrile (AIBN), glucose oxidase, glucose. Citric acid, monosodium phosphate, disodium phosphate, trisodium phosphate. dimethyl formamide (DMF), dimethylsulfoxide (DMSO), methanol, 2-propanol, hexane, ethyl acetate. 3-trimethyoxysilyl propyl methacrylate, acetic acid, ethanol were purchased from Sigma-Aldrich (St. Louis, MO, USA). 2-Methyl-1,4-phenylene bis(4-(3-(acryloyloxy)propoxy)benzoate) (RM 257) was purchased from Shijiazhuang Sdyano Fine Chemical, Co., Ltd. (Shijiazhuang, Hebei, China). 1,6-hexanedithiol (HDT), pentaerythritol tetrakis (3-mercaptopropionate) (PETMP), dipropylamine (DPA) and toluene were purchased from Sigma-Aldrich (St. Louis, MO, USA). Polydimethylsiloxane (PDMS) (Sylgard 184) was purchased from Dow Inc. (Midland, MI, USA). Silicone adhesive was purchased from Loctite (Düsseldorf, Germany). These chemicals were used directly as purchased, unless further specified.

UV LED (Dymax, Torrington, CT, USA), pH meter (Thermo Scientific, Waltham, MA, USA), Vacuum Oven (VWR, Radnor, PA, USA), Freeze Dryer (Labconco, Kansas City, MO, USA), Arduino (Arduino, Somerville, MA, USA), Profilometer (Bruker, Billerica, MA, USA), SEM (JEOL, Tokyo, Japan), FTIR (PerkinElmer, Waltham, MA, USA), Critical CO2 dryer (Tousimis, Rockville, MD, USA), Laser (green, 532 nm) and Laser (red, 650 nm) (Thorlabs, Newton, NJ, USA).

2.2. Synthesis of IIS Sensors

Hydrogel sensors were prepared by photopolymerization of aqueous monomer solutions following the fabrication process illustrated in Supplementary Figure S1. Monomers (acrylamide, N-isopropylacrylamide, acrylic acid, or 2-(dimethylamino)ethyl methacrylate) were combined with crosslinkers (Bis, PEGDA250, PEGDA525, or PEGDA700) and photoinitiators (Irgacure 2959, Darocur 1173, or TPO-Li) in deionized water. Formulations contained 10–60% *w*/*w* monomer and 1–4% *w*/*w* crosslinker relative to total solution mass.

For acrylamide-acrylic acid and NIPAm-Am systems, Bis crosslinker and Irgacure 2959 were maintained at 1% *w*/*w*. DMAEMA formulations utilized 0.7% *w*/*w* TPO-Li with various crosslinkers tested. PEGDA700 at 3% *w*/*w* was selected for final device fabrication based on consistent homogeneous polymerization and favorable swelling characteristics. Formulations with Bis crosslinker produced fragile gels, while those exceeding 60% monomer or 3% crosslinker content were excessively rigid despite ready polymerization.

For enzyme-responsive sensors, urease (Sigma-Aldrich, St. Louis, MO, USA) (0.4% *w*/*w*) or glucose oxidase (0.1–1% *w*/*w*) was dissolved in the monomer solution. Solutions were homogenized by stirring for 15 min. Aliquots of 160–500 µL were dispensed into PDMS molds (60–1500 µm depth) and covered with functionalized glass slides, avoiding air bubble entrapment. Acrylamide-based formulations were polymerized under 400 W UV illumination for 60 s using a Dymax 2000-EC Series flood lamp (Dymax, Torrington, CT, USA). DMAEMA formulations required 600 W UV LED exposure for 20 min. Polymerized films remained adhered to glass substrates upon demolding.

2.3. Functionalized Substrates

Glass substrates were cut to size and cleaned by sequential sonication in ethanol, acetone, and water (15 min each) using a Branson 5800 sonicator (Branson Ultrasonics, Danbury, CT, USA). After N_2 drying, substrates underwent O_2 plasma treatment (3 min, high power) in a Harrick Plasma PDC-001 cleaner (Harrick Plasma, Ithaca, NY, USA) (115V). Immediately following plasma exposure, substrates were immersed in a silanization solution containing ethanol (600 mL), acetic acid (18 mL, 10%), and 3-(trimethoxysilyl)propyl methacrylate (6 mL) for 48 h. Functionalized substrates were stored in a desiccator until use.

The silanization treatment with 3-(trimethoxysilyl)propyl methacrylate creates covalent bonds between the glass substrate and hydrogel network through copolymerization of the methacrylate groups during UV polymerization. This chemical anchoring mechanism has been demonstrated to provide exceptional interfacial stability, withstanding repeated swelling-deswelling cycles and long-term aqueous immersion without delamination [42]. Previous studies have shown that silanized interfaces maintain adhesion strength above 100

kPa even after 6 months of continuous water exposure, far exceeding the ~10 kPa stress generated during hydrogel swelling [43]. Furthermore, the transparent glass substrate requirement can be addressed through alternative transparent polymeric substrates (e.g., silanized PET or PMMA) that offer similar optical clarity while enabling flexible device architectures [44].

2.4. Soft Robotic LCE-Based Actuator

Liquid crystal elastomer (LCE) actuators were prepared following the protocol of Shi et al. [38]. Candle soot (CS) was collected on aluminum foil from burning paraffin candles. The LCE matrix was synthesized via two-step thiol-acrylate Michael addition. RM 257 monomer and Irgacure 2959 (0.6% *w*/*w*) were dissolved in toluene (30% *w*/*w*) and combined with PETMP (13 mol% of thiol groups), HDT (2.5% molar excess of acrylate), and CS (1.0% *w*/*w*). The mixture was stirred at 80 °C and 500 rpm, then sonicated for 20 min in a Branson 5800 bath sonicator.

DPA catalyst solution (1 mol% based on thiol groups, 2% *w*/*w* in toluene) was added dropwise with continuous stirring. The reaction mixture was cast between glass plates coated with Kapton tape (DuPont, Wilmington, DE, USA) and reacted at room temperature for 24 h, followed by 55 °C curing for an additional 24 h. The partially crosslinked film was stretched to 60% strain, clamped in the extended state, and exposed to 365 nm UV light for 30 min to complete crosslinking.

2.5. Characterization

Swelling ratios and surface morphologies were analyzed using a Nikon camera with Tracker (version 6.0.1) and ImageJ software (version 1.53) for image analysis. Elastic moduli were determined by dynamic mechanical analysis (DMA 850, TA Instruments, New Castle, DE, USA) at 8%/min strain rate and 25 °C. Optical properties were characterized using a Shimadzu UV-3101-PC UV-Vis-NIR (Shimadzu Corporation, Kyoto, Japan) spectrophotometer for transmission and reflectance measurements. Solution pH was monitored with a Thermo Scientific pH meter (Thermo Fisher Scientific, Waltham, MA, USA).

3. Result and Discussion

3.1. Surface Instability-Induced Optical Switching in Constrained Hydrogels

Substrate-constrained hydrogel films undergo surface instability formation when exposed to environmental stimuli (Figure 1a). In our PDMAEMA system, acidic conditions protonate tertiary amine groups, enhancing hydrophilicity and generating osmotic pressure that drives water uptake. The polymer network attempts to expand isotropically, but substrate adhesion prevents lateral expansion at the bottom interface. This geometric constraint converts volumetric swelling into compressive stress within the film plane. Once this stress exceeds the critical buckling threshold—determined by the film's elastic modulus and thickness—the surface spontaneously forms periodic wrinkles to minimize elastic energy [45–47]. Optical measurements reveal a dramatic transformation (Figure 1b,c): smooth films with >80% transmission at 650 nm suddenly develop light-scattering surface textures, reducing transmission below 20%. This transition occurs within 0.5 pH units, producing an unambiguous visual change from transparent to opaque states. The cooperative nature of polymer volume phase transitions ensures no intermediate states exist—sensors are either fully transparent or completely opaque, enabling reliable binary detection without instrumentation. Importantly, hysteresis characterization revealed minimal differences between forward and reverse pH sweeps (Supplementary Figure S2), with both normalized transmission and mass changes showing nearly overlapping profiles during acidification and alkalinization cycles. The sensors maintained consistent critical pH thresholds (pH 7–8.0) regardless of sweep direction, ensuring reliable and reproducible detection without drift in activation points—a critical requirement for practical sensing applications.

The robust substrate-hydrogel interface achieved through silane coupling ensures long-term operational stability of IIS sensors. The covalent Si-O-Si bonds formed during silanization are hydrolytically stable at pH 3–9, covering the entire operational range of our sensors. Wang et al. demonstrated that hydrogels anchored to glass substrates through siloxane bonds maintained firm adhesion in purified water and acidic solutions for over 36 days, only detaching in strongly alkaline conditions (pH > 9) [48]. This chemical anchoring prevents the interfacial failure modes commonly observed in physically adhered hydrogel films, such as delamination, edge lifting, or catastrophic peeling during volume phase transitions. Additionally, the constrained swelling mechanism inherently protects the interface—while unconstrained hydrogels can experience 300–400% volume changes that generate destructive stresses, substrate-constrained films redirect expansion perpendicular to the interface, minimizing shear forces that could compromise adhesion [49].

Systematic characterization across multiple hydrogel formulations revealed the parameter space governing instability formation (Figure 1d). Elastic modulus measurements using dynamic mechanical analysis showed values ranging from 65 kPa for 40%-3% monomer-crosslinker compositions to 425 kPa for 50%-2% formulations. Critical swelling ratios varied from 1.5 to 4.5, inversely correlating with crosslink density. For PDMAEMA systems, critical pH values shifted from 5.5 to 9.0 with increasing polymer content, while P(AAm-*co*-AAc) exhibited opposite trends due to anionic carboxylic groups [30]. P(NIPAm-*co*-Am) hydrogels responded to solvent polarity rather than pH, with critical transitions occurring at polarity indices between 3.8 and 4.5. Despite these diverse chemical mechanisms, all systems followed similar mechanical principles—surface instability occurred when swelling-induced stress exceeded approximately 0.3 times the elastic modulus. However, experimental testing revealed a critical limitation: wrinkled surfaces showed strong angular dependence in visibility. Sensors appearing transparent when viewed at oblique angles (e.g., 45°) displayed opaque wrinkled textures under perpendicular observation. Quantitative measurements confirmed transmission could vary by over 50% depending on observation angle, severely limiting applications where sensor orientation cannot be controlled [39,40].

Film thickness emerged as the key parameter determining both wrinkle formation and optical performance (Figure 1e). Finite element analysis revealed thickness controls surface pattern characteristics through two mechanisms. First, bending stiffness scales with thickness cubed, establishing the minimum stress required for buckling. Second, thickness determines the characteristic length scale of instability patterns. Simulations showed 300 μm films produce high-frequency wrinkles with 50–100 μm wavelengths, while 1500 μm films generate low-frequency undulations exceeding 200 μm wavelength. Experimental validation confirmed only films within 160–1300 μm thickness successfully formed visible wrinkles—thinner films experienced uniform stress preventing localized buckling, while thicker films required stresses beyond what swelling could generate. Most critically, spectroscopic analysis across 400–800 nm revealed that 300 μm thickness produces optimal light scattering (Figure 1f). At this thickness, wrinkle dimensions match visible light wavelengths, generating Mie scattering that appears uniformly opaque over a wide range of viewing angles. Combined transmission and 90° reflectance measurements showed angle-independent visibility metrics reached minimum values at 300 ± 50 μm thickness, reducing observation angle effects by over 80% compared to unoptimized sensors. This morphological control transforms IIS sensors into robust optical indicators suitable for integration with autonomous soft robotic systems.

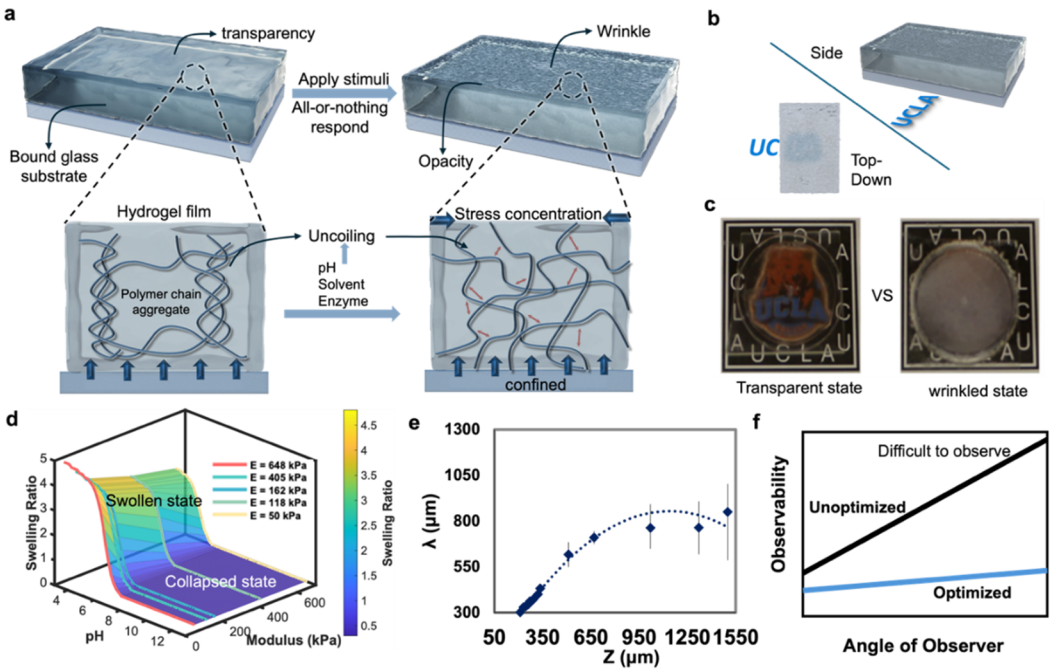

Figure 1. Fundamental mechanisms and design principles of IIS sensors. (**a**) Stimulus-induced transformation from coiled to confined polymer chains generating surface instabilities. (**b**) Fabricated IIS sensor with visual contrast indicator. (**c**) Transparent-to-opaque transition demonstrating naked-eye readability. (**d**) Three-parameter design space of modulus-pH-swelling relationships. (**e**) Finite element analysis of thickness-dependent wrinkle wavelength evolution. (**f**) Angular observability enhancement through thickness optimization.

3.2. Thickness-Mediated Transition from Angle-Dependent to Omnidirectional Visibility

Systematic variation of monomer-crosslinker ratios in PDMAEMA hydrogels produced sensors with distinct pH response thresholds (Figure 2a). Visual inspection revealed wrinkle formation occurring at pH values ranging from 3.5 to 10.0 across different formulations (Supplementary Figure S3). Quantitative transmission measurements at 650 nm confirmed these observations, showing sharp optical transitions within 0.5 pH units (Figure 2b). Each sensor formulation exhibited characteristic critical pH values: 40%-3% M-CL compositions activated at pH 3.5, while 50%–2% formulations required pH 8.0 for wrinkle formation (Figure 2c). These extracted parameters, combined with elastic modulus measurements (65–425 kPa from DMA analysis) (Supplementary Figure S4) and swelling ratio determinations (1.5–4.5), enabled construction of a comprehensive design space (Figure 2d). The normalized pH metric (pHBP) successfully integrated data from both cationic PDMAEMA and anionic P(AAm-*co*-AAc) systems, which exhibit opposite pH responses [30]. This three-dimensional parameter space accurately predicted instability thresholds across diverse polymer chemistries. However, sensors with identical polymer compositions occasionally showed inconsistent optical responses, suggesting additional factors influenced performance.

Film thickness emerged as the critical factor explaining performance variations. Systematic studies across 60–1500 μm thicknesses revealed that only films within 160–1300 μm consistently produced visible wrinkles upon pH stimulation (Figure 2e). Time-resolved transmission measurements demonstrated distinct thickness-dependent behaviors: 160 μm films showed rapid but modest transmission changes (ΔT ~20%), 300–650 μm films exhibited pronounced drops (ΔT > 70%), while 1300 μm films displayed delayed, gradual responses. Films thinner than 160 μm failed to wrinkle due to substrate constraint dominating the entire film thickness, preventing stress localization necessary for buckling. Films exceeding 1300 μm required prohibitively high stresses for instability formation, as bending rigidity scales with thickness cubed [50]. Additionally, thicker films suffered from extended diffusion times that prevented sharp pH gradients needed for localized stress generation. Within the operational range, another critical issue emerged: sensors showed strong viewing angle dependence. Films appearing transparent at 45° oblique angles displayed opaque wrinkled textures under perpendicular observation, with transmission varying by over 50% based on viewing geometry.

Finite element analysis provided mechanistic insights into thickness-dependent wrinkle formation (Figure 2f). The coupled diffusion-deformation model incorporated hygroscopic swelling:

$$\varepsilon_{hs} = \beta M_m (C - C_{ref}) \quad (1)$$

where ε_{hs} represents the hygroscopic strain, M_m is the molar mass, and C and C_{ref} are the concentrations inside the hydrogel and reference concentration, respectively [51–53]. Simulations revealed systematic evolution of surface morphology with thickness: 300 μm films produced high-frequency wrinkles (λ = 50–100 μm) with modest amplitudes (~50 μm), 650 μm films showed intermediate patterns (λ = 100–150 μm), and 1500 μm films generated low-frequency undulations (λ > 200 μm) with amplitudes exceeding 200 μm. The wavelength-thickness relationship followed $\lambda \propto h^{0.8}$, consistent with elastic instability theory. Experimental profilometry confirmed these predictions (Supplementary Figure S5). Interestingly, wrinkle morphology transitioned from herringbone patterns in 180–250 μm films to labyrinthine structures in 280–350 μm films (Supplementary Figure S6), though both geometries produced equivalent light scattering. Wavelength-resolved transmission measurements across 400–800 nm showed thickness-dependent kinetics, with 300 μm films achieving 90% of their final opacity within 2 min, compared to over 10 min for 1300 μm films (Figure 2g).

Comprehensive optical characterization revealed the mechanism underlying angle-independent detection. While transmission measurements alone suggested multiple potentially optimal thicknesses, incorporating 90° reflectance data provided the complete picture (Figure 2h). Thin films (160 μm) showed minimal reflectance changes despite transmission drops, indicating light passed through wrinkled regions rather than scattering. Thick films (1300 μm) exhibited high baseline reflectance that masked wrinkle-induced changes. Films near 300 μm thickness demonstrated maximum changes in both transmission (ΔT = 75%) and reflectance (ΔR = 45%), indicating efficient multi-directional light scattering. The combined angle independence metric:

$$\text{Angle Independence} = (R_f + T_f)/(R_i + T_i) \quad (2)$$

where subscripts f and i denote final (wrinkled) and initial (clear) states, reached its minimum at 300 ± 50 μm thickness (Figure 2i). This optimal performance arises from wrinkle dimensions at this thickness matching visible light wavelengths, producing Mie scattering that appears uniformly opaque regardless of observation angle [54–57]. Temperature-controlled experiments confirmed these films maintained consistent visibility from 0° to 60° viewing angles, substantially reducing the orientation constraints that limited previous IIS sensors. Visual comparison of sensors with different thicknesses clearly demonstrates this thickness-dependent angular visibility

(Supplementary Figure S7). Sensors with non-optimal thicknesses (160 μm and 650 μm) exhibit pronounced transparency variations when viewed from different angles—appearing transparent at certain viewing angles while showing partial opacity at others. In contrast, the optimized 300 μm thickness sensors maintain consistent opacity across the entire 0°–60° viewing range, with minimal variation in visual appearance regardless of observation angle. While not achieving complete omnidirectional visibility (360°), this represents a significant advancement over our previous work [26] which required precise oblique viewing angles (45° ± 5°) for reliable detection. This four-parameter framework—incorporating elastic modulus, swelling ratio, critical stimulus concentration, and film thickness—enables rational design of sensors with predetermined thresholds and reliable omnidirectional visibility.

Long-term cycling tests further validated the practical viability of these sensors (Supplementary Figure S8). Over 100 operational cycles, sensors demonstrated exceptional durability with >85% retention of their initial transmission range. Specifically, sensors cycled between water (pH = 1) and hexane maintained 91.0% of their optical response range, while those alternating between pH 7 and pH 8 environments retained 92.6% of their performance metrics. The minimal performance degradation and consistent activation thresholds throughout extended cycling confirm that the surface instability mechanism remains robust despite repeated mechanical deformations, supporting applications in reusable logic gates and autonomous control systems.

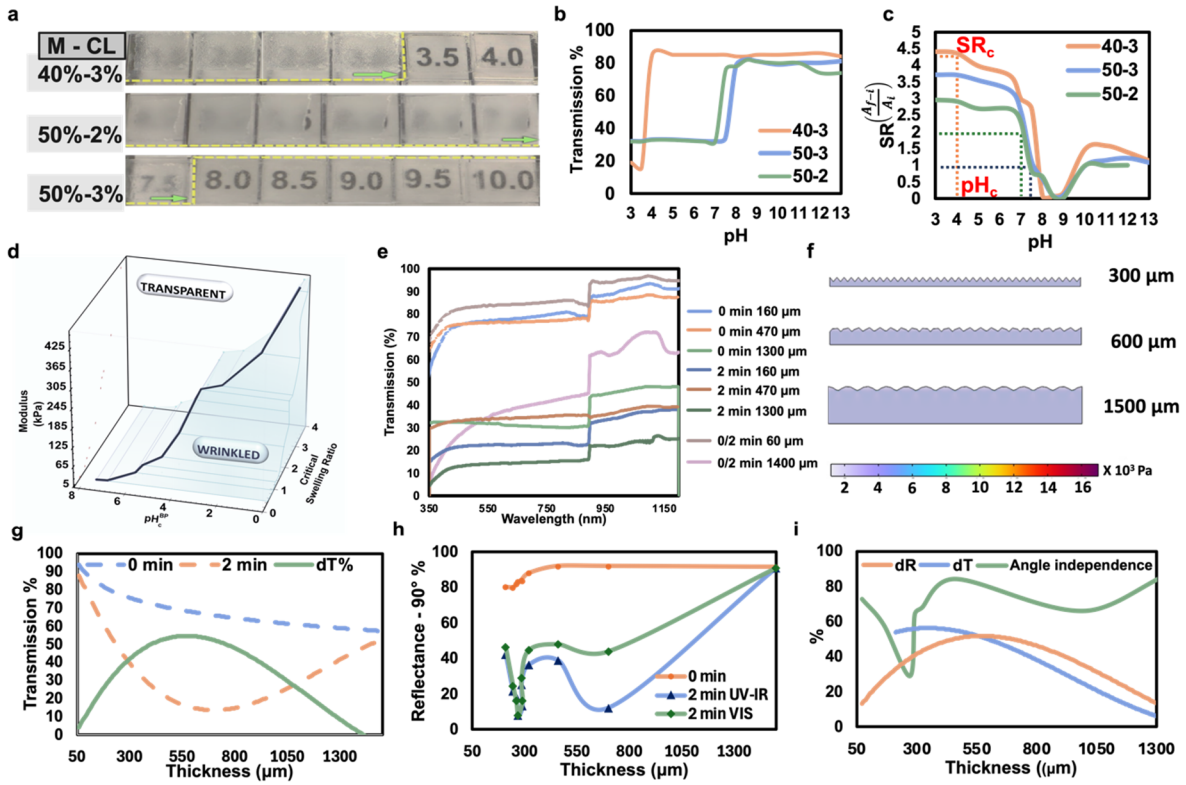

Figure 2. Systematic optimization of IIS sensor parameters. (**a**) Photographic array of pH-responsive sensor strips with varied monomer-crosslinker formulations displaying concentration-dependent opacity. (**b**) UV-Vis transmission spectra demonstrating abrupt intensity drops at formulation-specific pH thresholds. (**c**) Critical pH thresholds and corresponding swelling ratio determinations. (**d**) Normalized three-dimensional design space for universal polymer systems. (**e**) Temporal evolution of optical transmission across thickness range. (**f**) Finite element simulations of surface displacement profiles across three representative thicknesses. (**g**) Spectral transmission data comparing wavelength-independent responses. (**h**) Reflectance measurements at 90-degree collection angle for comprehensive optical characterization. (**i**) Angle-independence optimization revealing optimal 300 μm thickness.

3.3. Enzymatic pH Modulation and Polymer-Solvent Interaction-Based Detection Systems

Enzyme-coupled IIS sensors exploit a unique signal amplification mechanism where single glucose molecules generate multiple protons through Glucose Oxidase (Gox) catalysis (Figure 3a) [58,59]. The enzymatic cascade (glucose + O_2 → gluconic acid + H_2O_2) creates steep pH gradients within the hydrogel matrix, dropping from physiological pH to ~2 near enzyme sites [49,50]. This localized acidification is crucial—bulk pH changes would require impractically high glucose concentrations, but compartmentalized reactions within the polymer network achieve threshold swelling at clinically relevant levels. Unexpectedly, enzyme loading showed biphasic

effects on sensor performance: swelling increased until 0.2% *w*/*w* GOx, then declined at higher loadings (Supplementary Figure S9). This counterintuitive behavior reveals competing mechanisms—while more enzyme generates more acid, excessive protein content creates physical crosslinks that restrict polymer chain mobility. The optimal 0.2% *w*/*w* loading balances catalytic activity with mechanical compliance, enabling sensors to detect glucose across 200–1000 mg/dL ranges relevant to diabetes monitoring (Figure 3b).

The power of array-based sensing lies not in individual sensor precision but in collective information encoding. Each sensor element functions as a chemical comparator, switching states only when glucose exceeds its preset threshold (Figure 3c). By engineering systematic threshold variations through polymer content (40–50% *w*/*w*), we created a biological analog-to-digital converter: continuous glucose concentrations transform into discrete visual patterns. The array's stepped activation profile (Figure 3d) mirrors clinical glucose ranges—single sensor activation (200–400 mg/dL) indicates hypoglycemia requiring immediate intervention, two sensors (600–800 mg/dL) confirm normal fasting levels, while complete activation (>1000 mg/dL) warns of dangerous hyperglycemia. This design philosophy prioritizes actionable information over numerical precision. Unlike digital glucometers providing exact values that users must interpret, IIS arrays directly communicate clinical status through intuitive visual patterns, particularly valuable in resource-limited settings where device maintenance and user training present barriers.

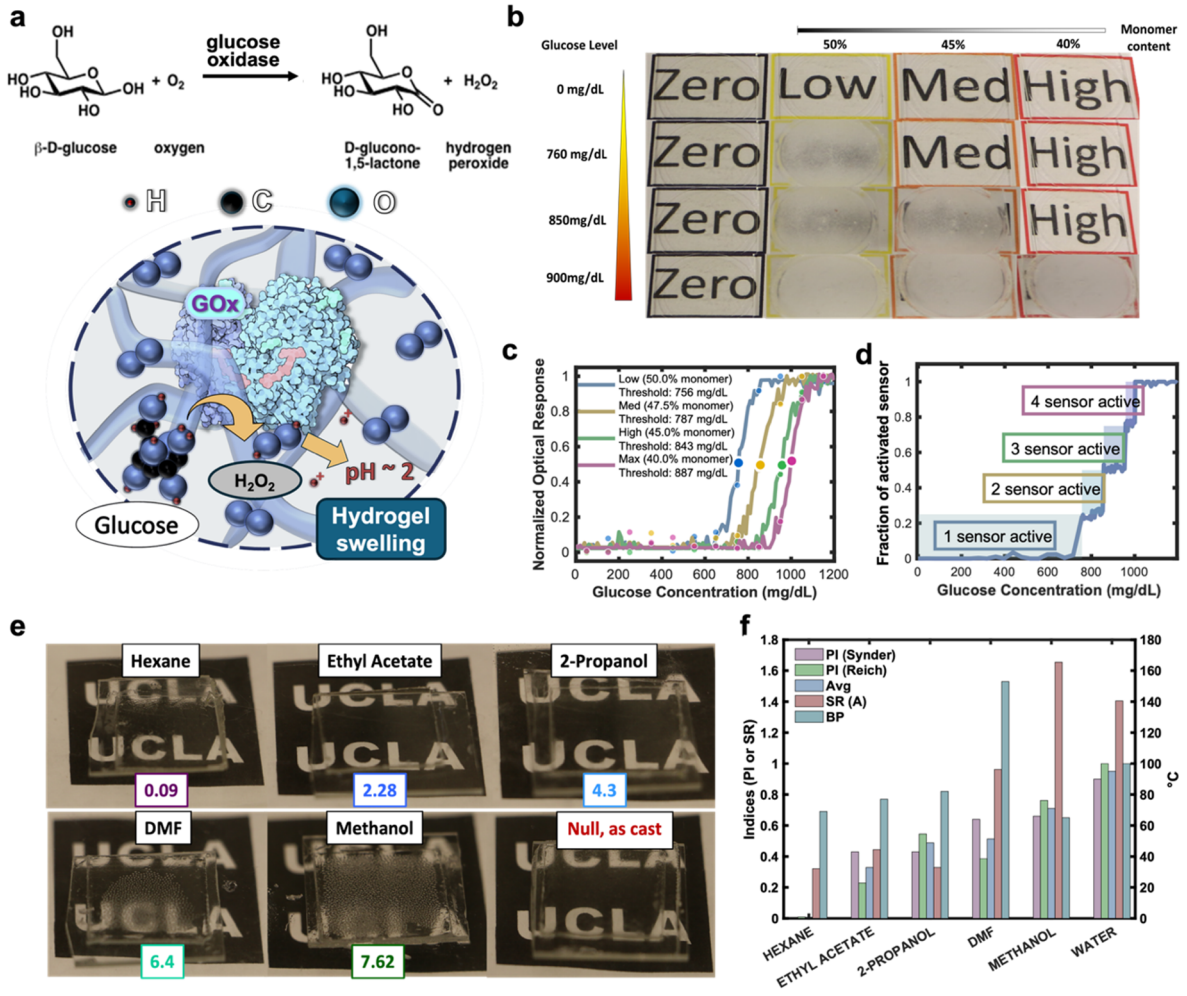

Figure 3. Multi-stimuli sensing applications. (**a**) Glucose oxidase-catalyzed conversion of glucose to gluconic acid inducing pH-triggered hydrogel swelling. (**b**) Semi-quantitative glucose detection array with differential activation thresholds across clinical concentration ranges. (**c**) Normalized optical responses of sensors with systematically varied glucose sensitivities. (**d**) Collective sensor activation pattern for concentration range identification. (**e**) Selective optical response to solvents of varying polarity indices. (**f**) Quantitative correlation between solvent polarity parameters and hydrogel swelling behavior.

Direct polarity sensing reveals fundamental differences in stimulus-response mechanisms between enzyme-coupled and physical detection modalities (Figure 3e). P(NIPAm-*co*-Am) hydrogels exhibit threshold behavior at PI ~3.5 [60,61], below which polymer-polymer interactions dominate, maintaining collapsed conformations

despite solvent exposure. Above this threshold, solvent molecules disrupt hydrophobic associations, triggering cooperative swelling transitions. The sharp discrimination between transparent (PI < 3.5) and opaque (PI > 3.5) states enables binary solvent classification without gradual transitions (Figure 3f). Remarkably, this threshold remains consistent across diverse solvent classes—alcohols, amides, and water—suggesting the response depends on general solvation power rather than specific molecular interactions (Supplementary Figure S10). This universality extends to mixed solvents, where sensors respond to volume-averaged polarity rather than preferentially interacting with either component (Supplementary Figure S11). The ability to transduce both biochemical reactions and physical properties through identical optical outputs demonstrates the versatility of surface instability as a signal transduction mechanism, enabling multiplexed arrays that simultaneously monitor diverse environmental parameters (Supplementary Figure S12).

3.4. Soft Material Logic Gates for Autonomous Control of LCE Actuators

IIS sensors exhibit intrinsic Boolean behavior through their threshold-dependent optical transitions, making them natural candidates for material-based computation (Figure 4a). Unlike gradual responses that require complex signal processing, the abrupt transparent-to-opaque switching at critical stimuli concentrations creates unambiguous binary states. This eliminates the need for analog-to-digital conversion—the material itself performs the digitization. Environmental stimuli (pH changes, solvent exposure) replace voltage inputs in classical logic gates, while optical transmission substitutes for current output. The fundamental advantage lies in passive operation: no power supply, clock signals, or refresh cycles are required. Ambient light serves as both the signal carrier and energy source, with hydrogel states storing information through mechanical deformation rather than charge separation. This approach transforms traditionally active electronic components into passive material elements that compute through their physical response to environmental conditions.

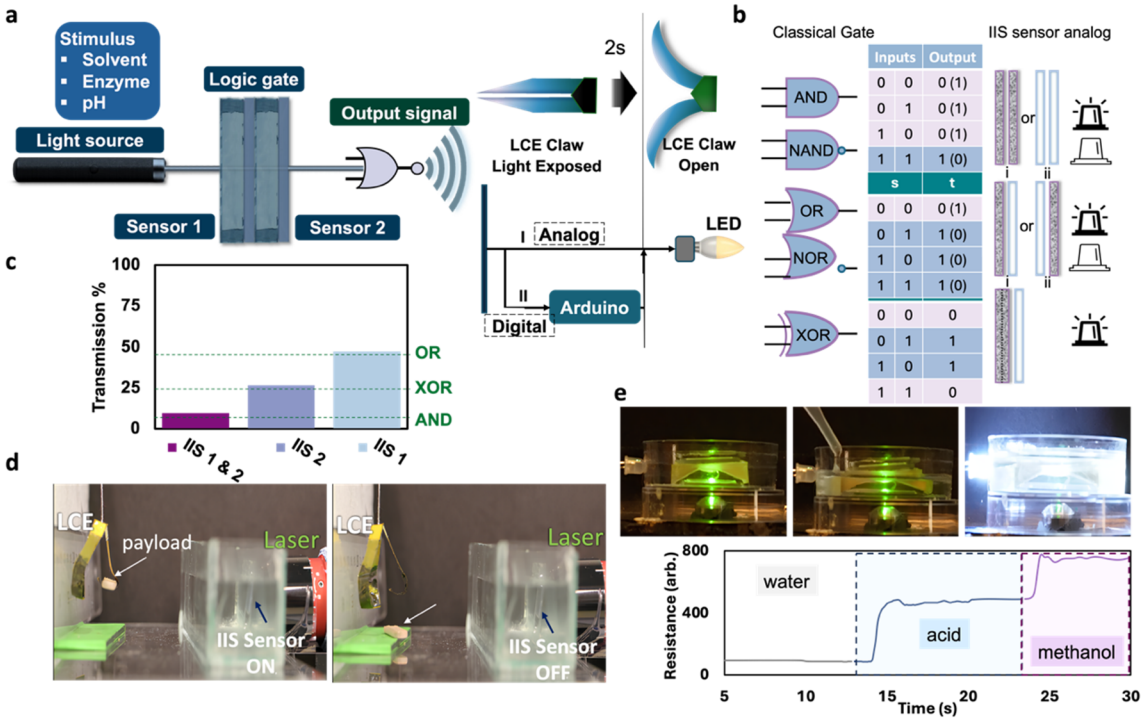

Figure 4. Logic gate implementation and autonomous control. (**a**) Integration of IIS sensors as computational elements for stimulus-responsive actuation of soft robotic and electronic systems. (**b**) Boolean operation mapping from voltage-based to environment-based logic gates. (**c**) Threshold-dependent optical transmission establishing distinct logic states for OR, XOR, and AND operations. (**d**) Autonomous LCE gripper actuation via laser transmission modulation through IIS optical switching. (**e**) Sequential environmental stimuli processing in pH-polarity AND gate configuration with conditional LED activation.

Systematic optical characterization established the transmission thresholds required for different Boolean operations (Figure 4b,c). Single IIS sensors functioning as pass-through elements maintained 80% transmission in the OFF state, dropping to 20% when activated. Stacking sensors in series created AND gate functionality, with combined transmission falling to 10% only when both sensors activated. Parallel sensor arrangements with partial

overlap produced OR gates exhibiting 50% transmission when either sensor triggered. Most intriguingly, offset sensor pairing generated XOR behavior—25% transmission occurred when only one sensor activated, while dual activation restored higher transmission through spatial light redistribution. These distinct optical signatures remained consistent across 400–800 nm wavelengths (Supplementary Figure S13b), ensuring robust operation under varied lighting conditions. The 15 s switching time, limited by polymer swelling kinetics rather than electronic delays, proves adequate for environmental monitoring applications where stimuli change over minutes to hours.

Autonomous actuation demonstrations validated practical implementation in both soft robotic and electronic systems. LCE grippers programmed with nematic-to-isotropic transition temperatures of 45 °C responded to 650 nm laser heating modulated by IIS optical gates (Figure 4d). In the wrinkled ON state, sensors blocked laser transmission, maintaining gripper closure and payload retention. Environmental stimuli switching sensors to transparent OFF states enabled laser penetration, heating LCE above transition temperature to induce 40% contraction and payload release. This configuration achieved stimulus-triggered mechanical work without control circuitry, batteries, or wireless communication. Electronic integration through photoresistor interfaces demonstrated more complex operations (Figure 4e). An AND gate combining pH-sensitive (threshold pH 6) and polarity-sensitive (threshold PI 4.0) sensors required both acidic conditions and polar solvent exposure to activate LED output. Sequential exposure to water (pH 7, PI 9), acid (pH 3, PI 9), and finally acid plus methanol (pH 3, PI 5) confirmed proper AND logic—only the dual-stimulus condition triggered the 760-unit resistance threshold for LED activation. The modular architecture enables construction of multi-input gates and cascaded logic circuits through standardized sensor elements (Supplementary Figure S13c,d), suggesting pathways toward fully soft, environmentally responsive computational systems.

4. Conclusions

The discovery that film thickness controls both wrinkle morphology and optical scattering in IIS sensors resolves a fundamental limitation of surface instability-based detection—angle-dependent visibility that has restricted practical deployment. By optimizing thickness to 300 μm, where wrinkle dimensions match visible light wavelengths, omnidirectional sensors emerge that maintain consistent appearance regardless of viewing geometry. This morphological control, combined with the intrinsic threshold response of stimuli-responsive hydrogels, enables a conceptual leap from passive indicators to active computational elements. The demonstration of soft material logic gates—while currently limited by 15 s switching speeds suitable for environmental monitoring rather than rapid computation—establishes that information processing need not require electrons, power supplies, or rigid semiconductors. Instead, mechanical deformation can encode binary states, ambient light can carry signals, and polymer swelling can execute Boolean operations. The enzymatic glucose sensors achieving clinical range detection (200–1000 mg/dL) and solvent polarity discriminators operating at PI ~3.5 thresholds validate the versatility of this approach across biochemical and physical sensing modalities. Most significantly, integrating these capabilities with autonomous LCE actuators proves that entirely soft systems can sense, decide, and respond without electronic mediation. Future advances will focus on reducing response times through thinner active layers, expanding stimulus vocabulary through multi-responsive polymers, and developing hierarchical architectures where local material computations coordinate to produce emergent behaviors.

Supplementary Materials: The following supporting information can be downloaded at: https://media.sciltp.com/articles/others/2509041550542777/MI-1420-SI-revised.pdf, including additional characterization data, Supplementary Figures S1–S13.

Author Contributions: R.K. and I.F. contributed equally to this work. R.K. assisted with data interpretation, and contributed to manuscript writing. I.F. conceived the concept, designed experiments, performed mechanical characterization, performed synthesis, developed the multi-stimuli systems, and conducted data analysis. Z.L. assisted with COMSOL simulations and theoretical modeling. C.W.Z. and P.H. assisted with data interpretation. P.S. developed the LCE actuator system and performed soft robotic demonstrations. Y.A. contributed to the initial pH-responsive system development. Y.D., S.D. and D.W. performed supporting experiments and characterization. A.J. assisted with data collection and provided support in materials preparation. M.H. and S.W. provided technical guidance on hydrogel synthesis and characterization methods. X.H. supervised the project, secured funding, and edited the manuscript. All authors reviewed and approved the final manuscript.

Funding: This research was funded by the American Chemical Society, grant number 66747-ND7; Johnson & Johnson, grant number 20231448; Inventor Fellow, grant number 12072; National Institutes of Health (NIH), grant number R01DK132319; Gordon and Betty Moore Foundation, grant number 12072; Semiconductor Research Corporation, grant number 2023-JU-3136; and the Office of Naval Research (ONR), grant numbers N000142412187 and N000142212595.

Data Availability Statement: Not applicable. Requests for data may be made to the corresponding author under appropriate justification.

Acknowledgments: The authors gratefully acknowledge financial support from the American Chemical Society, Johnson & Johnson, Inventor Fellow program, NIH, the Moore Foundation, Semiconductor Research Corporation, and the Office of Naval Research.

Conflicts of Interest: The authors declare no conflict of interest.

References

1. Ates, H.C.; Nguyen, P.Q.; Gonzalez-Macia, L.; Morales-Narvaez, E.; Guder, F.; Collins, J.J.; Dincer, C. End-to-end design of wearable sensors. *Nat. Rev. Mater*. **2022**, *7*, 887–907.
2. Zhao, D.; Zhu, Y.; Cheng, W.; Chen, W.; Wu, Y.; Yu, H. Cellulose-Based Flexible Functional Materials for Emerging Intelligent Electronics. *Adv. Mater*. **2021**, *33*, e2000619.
3. McEvoy, M.A.; Correll, N. Materials science. Materials that couple sensing, actuation, computation, and communication. *Science* **2015**, *347*, 1261689.
4. Qian, X.; Zhao, Y.; Alsaid, Y.; Wang, X.; Hua, M.; Galy, T.; Gopalakrishna, H.; Yang, Y.; Cui, J.; Liu, N.; et al. Artificial phototropism for omnidirectional tracking and harvesting of light. *Nat. Nanotechnol*. **2019**, *14*, 1048–1055.
5. Pedro, D.I.; Nguyen, D.T.; Trachsel, L.; Rosa, J.G.; Chu, B.; Eikenberry, S.; Sumerlin, B.S.; Sawyer, W.G. Superficial Modulus, Water-Content, and Mesh-Size at Hydrogel Surfaces. *Tribol. Lett*. **2021**, *69. 160.*
6. Zhao, Y.; Lo, C.Y.; Ruan, L.; Pi, C.H.; Kim, C.; Alsaid, Y.; He, X. Somatosensory actuator based on stretchable conductive photothermally responsive hydrogel. *Sci. Robot.* **2021**, *6*, eabd5483.
7. Zhao, Y.; Hua, M.; Yan, Y.; Wu, S.; Alsaid, Y.; He, X. Stimuli-Responsive Polymers for Soft Robotics. *Annu. Rev. Control Robot. Auton. Syst*. **2022**, *5*, 515–545.
8. Hoffman, A.S. Hydrogels for biomedical applications. *Adv. Drug Deliv. Rev.* **2012**, *64*, 18–23.
9. Cai, Z.; Luck, L.A.; Punihaole, D.; Madura, J.D.; Asher, S.A. Photonic crystal protein hydrogel sensor materials enabled by conformationally induced volume phase transition. *Chem. Sci*. **2016**, *7*, 4557–4562.
10. Dušková-Smrčková, M.; Dušek, K. How to Force Polymer Gels to Show Volume Phase Transitions. *ACS Macro Lett*. **2019**, *8*, 272–278.
11. Walker, J.P.; Asher, S.A. Acetylcholinesterase-Based Organophosphate Nerve Agent Sensing Photonic Crystal. *Anal. Chem*. **2005**, *77*, 1596–1600.
12. Ferreira, L.; Vidal, M.M.; Gil, M.H. Evaluation of poly(2-hydroxyethyl methacrylate) gels as drug delivery systems at different pH values. *Int. J. Pharm*. **2000**, *194*, 169–180.
13. Nakayama, M.; Yamada, N.; Kumashiro, Y.; Kanazawa, H.; Yamato, M.; Okano, T. Thermoresponsive poly(N-isopropylacrylamide)-based block copolymer coating for optimizing cell sheet fabrication. *Macromol. Biosci.* **2012**, *12*, 751–760.
14. Yetisen, A.K.; Jiang, N.; Fallahi, A.; Montelongo, Y.; Ruiz-Esparza, G.U.; Tamayol, A.; Zhang, Y.S.; Mahmood, I.; Yang, S.-A.; Kim, K.S.; et al. Glucose-sensitive hydrogel optical fibers functionalized with phenylboronic acid. *Adv. Mater*. **2017**, *29*, 1606380.
15. Choi, M.; Humar, M.; Kim, S.; Yun, S.-H. Step-Index Optical Fiber Made of Biocompatible Hydrogels. *Adv. Mater*. **2015**, *27*, 4081–4086.
16. Wang, Z.; Zhang, W.; Liu, X.; Li, M.; Lang, X.; Singh, R.; Marques, C.; Zhang, B.; Kumar, S. Novel Optical Fiber-Based Structures for Plasmonics Sensors. *Biosensors* **2022**, *12*, 1016.
17. Ling, Z.; Chen, J.; Li, S.; Lu, H.; Du, J.; Liu, Z.; Qiu, J. A multi-band stealth and anti-interference superspeed light-guided swimming robot based on multiscale bicontinuous three-dimensional network. *Chem. Eng. J*. **2024**, *485*, 150094.
18. Zhang, C.W.; Chen, C.; Duan, S.; Yan, Y.; He, P.; He, X. Hydrogel-based soft bioelectronics for personalized healthcare. *Med-X* **2024**, *2*, 20.
19. Yang, S.; Sarkar, S.; Xie, X.; Li, D.; Chen, J. Application of Optical Hydrogels in Environmental Sensing. *Energy Environ. Mater*. **2024**, *7*, e12646.
20. Cao, H.; Duan, L.; Zhang, Y.; Cao, J.; Zhang, K. Current hydrogel advances in physicochemical and biological response-driven biomedical application diversity. *Signal Transduct. Target. Ther*. **2021**, *6*, 426.
21. Yetisen, A.K.; Butt, H.; Volpatti, L.R.; Pavlichenko, I.; Humar, M.; Kwok, S.J.J.; Koo, H.; Kim, K.S.; Naydenova, I.; Khademhosseini, A.; et al. Photonic hydrogel sensors. *Biotechnol. Adv*. **2016**, *34*, 250–271.
22. Wang, M.; Yang, Y.; Min, J.; Song, Y.; Tu, J.; Mukasa, D.; Ye, C.; Xu, C.; Heflin, N.; McCune, J.S.; et al. A wearable electrochemical biosensor for the monitoring of metabolites and nutrients. *Nat. Biomed. Eng.* **2022**, *6*, 1225–1235.
23. Sun, S.; Chen, J. Recent Advances in Hydrogel-Based Biosensors for Cancer Detection. *ACS Appl. Mater. Interfaces* **2024**, *16*, 46988–47002.
24. Shen, P.; Li, M.; Li, R.; Han, B.; Ma, H.; Hou, X.; Zhang, Y.; Wang, J.-J. Aptamer-functionalized smart photonic hydrogels: application for the detection of thrombin in human serum. *NPG Asia Mater*. **2022**, *14*, 94.

25. Qin, M.; Sun, M.; Hua, M.; He, X. Bioinspired structural color sensors based on responsive soft materials. *Curr. Opin. Solid State Mater. Sci*. **2019**, *23*, 13–27.
26. Qin, M.; Sun, M.; Bai, R.; Mao, Y.; Qian, X.; Sikka, D.; Zhao, Y.; Qi, H.J.; Suo, Z.; He, X. Bioinspired Hydrogel Interferometer for Adaptive Coloration and Chemical Sensing. *Adv. Mater*. **2018**, *30*, 1800468.
27. Yang, S.; Tang, Z.; Tian, Y.; Ji, X.; Wang, F.; Xie, C.; He, Z. Dual-Color Fluorescent Hydrogel Microspheres Combined with Smartphones for Visual Detection of Lactate. *Biosensors* **2022**, *12*, *802.*
28. Li, W.; Zhang, X.; Hu, X.; Shi, Y.; Li, Z.; Huang, X.; Zhang, W.; Zhang, D.; Zou, X.; Shi, J. A smartphone-integrated ratiometric fluorescence sensor for visual detection of cadmium ions. *J. Hazard. Mater.* **2021**, *408*, 124872.
29. Wang, Q.; Zhao, X. Beyond wrinkles: Multimodal surface instabilities for multifunctional patterning. *MRS Bull*. **2016**, *41*, 115–122.
30. Frenkel, I.; Hua, M.; Alsaid, Y.; He, X. Self-Reporting Hydrogel Sensors Based on Surface Instability-Induced Optical Scattering. *Adv. Photonics Res*. **2021**, *2*, 2100058.
31. Fan, W.; Zeng, J.; Gan, Q.; Ji, D.; Song, H.; Liu, W.; Shi, L.; Wu, L. Iridescence-controlled and flexibly tunable retroreflective structural color film for smart displays. *Sci. Adv.* **2019**, *5*, eaaw8755.
32. Lee, K.-L.; Chang, C.-C.; You, M.-L.; Pan, M.-Y.; Wei, P.-K. Enhancing Surface Sensing Sensitivity of Metallic Nanostructures using Blue-Shifted Surface Plasmon Mode and Fano Resonance. *Sci. Rep*. **2018**, *8*, 9762.
33. Zhang, R.; Yang, Z.; Wang, Q.; Li, W.; Xu, H.; Li, L. Angle dependent structural colors with full-visible-spectrum and narrow-angle change properties for anti-counterfeiting. *Dyes Pigm*. **2023**, *208*, 110794.
34. Chung, J.Y.; Nolte, A.J.; Stafford, C.M. Surface Wrinkling: A Versatile Platform for Measuring Thin-Film Properties. *Adv. Mater*. **2011**, *23*, 349–368.
35. Warren, T.J.; Bowles, N.E.; Donaldson Hanna, K.; Bandfield, J.L. Modeling the Angular Dependence of Emissivity of Randomly Rough Surfaces. *J. Geophys. Res. Planets* **2019**, *124*, 585–601.
36. Gross, P.; Störzer, M.; Fiebig, S.; Clausen, M.; Maret, G.; Aegerter, C.M. A precise method to determine the angular distribution of backscattered light to high angles. *Rev. Sci. Instrum*. **2007**, *78*, 033105.
37. Considine, P.S.; Cronin, D.J.; Reynolds, G.O. Angular Dependence of Radiance of Rough Surfaces in Imaging Systems. *J. Opt. Soc. Am*. **1966**, *56*, 877–883.
38. Chen, C.; Shi, P.; Liu, Z.; Duan, S.; Si, M.; Zhang, C.; Du, Y.; Yan, Y.; White, T.J.; Kramer-Bottiglio, R.; et al. Advancing physical intelligence for autonomous soft robots. *Sci. Robot*. **2025**, *10*, eads1292.
39. Zhao, Y.; Li, Q.; Liu, Z.; Alsaid, Y.; Shi, P.; Jawed, M.K.; He, X. Sunlight-powered self-excited oscillators for sustainable autonomous soft robotics. *Sci. Robot*. **2023**, *8*, eadf4753.
40. Liu, Y.; Tian, G.; Du, Y.; Shi, P.; Li, N.; Li, Y.; Qin, Z.; Jiao, T.; He, X. Highly Stretchable, Low-Hysteresis, and Adhesive TA@MXene-Composited Organohydrogels for Durable Wearable Sensors. *Adv. Funct. Mater*. **2024**, *34*, 2315813.
41. Zhao, K.; Cao, X.; Alsaid, Y.; Cheng, J.; Wang, Y.; Zhao, Y.; He, X.; Zhang, S.; Niu, W. Interactively mechanochromic electronic textile sensor with rapid and durable electrical/optical response for visualized stretchable electronics. *Chem. Eng. J.* **2021**, *426*, 130870.
42. Liu, Q.; Nian, G.; Yang, C.; Qu, S.; Suo, Z. Bonding dissimilar polymer networks in various manufacturing processes. *Nat. Commun*. **2018**, *9*, 846.
43. Yuk, H.; Zhang, T.; Lin, S.; Parada, G.A.; Zhao, X. Tough bonding of hydrogels to diverse non-porous surfaces. *Nat. Mater*. **2016**, *15*, 190–196.
44. Wirthl, D.; Pichler, R.; Drack, M.; Kettlguber, G.; Moser, R.; Gerstmayr, R.; Hartmann, F.; Bradt, E.; Kaltseis, R.; Kaltenbrunner, M. Instant tough bonding of hydrogels for soft machines and electronics. *Sci. Adv*. **2017**, *3*, e1700053.
45. Vandeparre, H.; Gabriele, S.; Brau, F.; Gay, C.; Parker, K.K.; Damman, P. Hierarchical wrinkling patterns. *Soft Matter*. **2010**, *6*, 5751–5756.
46. Li, B.; Cao, Y.-P.; Feng, X.-Q.; Gao, H. Mechanics of morphological instabilities and surface wrinkling in soft materials: a review. *Soft Matter*. **2012**, *8*, 5728–5745.
47. Kim, H.S.; Crosby, A.J. Solvent-Responsive Surface via Wrinkling Instability. *Adv. Mater*. **2011**, *23*, 4188–4192.
48. Liu, J.; Jiang, Z.; Li, Y.; Kang, G.; Qu, S. Stability of hydrogel adhesion enabled by siloxane bonds. *Eng. Fract. Mech*. **2022**, *271*, 108662.
49. Kang, M.K.; Huang, R. Effect of surface tension on swell-induced surface instability of substrate-confined hydrogel layers. *Soft Matter*. **2010**, *6*, 5736–5745.
50. Auguste, A.; Yang, J.; Jin, L.; Chen, D.; Suo, Z.; Hayward, R.C. Formation of high aspect ratio wrinkles and ridges on elastic bilayers with small thickness contrast. *Soft Matter.* **2018**, *14*, 8545–8551.
51. Zhou, Y.; Chen, Y.; Jin, L. Three-dimensional postbuckling analysis of thick hyperelastic tubes. *J. Mech. Phys. Solids* **2023**, *173*, 105202.
52. Kang, C.; Liu, Z.; Chen, S.; Jiang, X. Circular trajectory weaving welding control algorithm based on space transformation principle. *J. Manuf. Process*. **2019**, *46*, 328–336.

53. Jin, L.; Takei, A.; Hutchinson, J.W. Mechanics of wrinkle/ridge transitions in thin film/substrate systems. *J. Mech. Phys. Solids* **2015**, *81*, 22–40.
54. Lynch, D.K. Snell's window in wavy water. *Appl. Opt*. **2015**, *54*, B8–B11.
55. Young, A.T. Rayleigh scattering. *Appl. Opt*. **1981**, *20*, 533–535.
56. Schwartz, C.; Dogariu, A. Conservation of angular momentum of light in single scattering. *Opt. Express*. **2006**, *14*, 8425–8433.
57. Mansuripur, M. Angular Momentum Exchange Between Light and Material Media Deduced from the Doppler Shift. *Proc. SPIE* **2012**, *8458*, 20–27.
58. Zia, M.A.; Khalil Ur, R.; Kamal, S.M.; Andaleeb, F.; Mahmood, I.R.; Ahmad, S.M.; Khan, I.A.; Ahmad, I.K. Thermal Characterization of Purified Glucose Oxidase from A Newly Isolated Aspergillus Niger UAF-1. *J. Clin. Biochem. Nutr*. **2007**, *41*, 132–138.
59. Bright, H.J.; Appleby, M. The pH Dependence of the Individual Steps in the Glucose Oxidase Reaction. *J. Biol. Chem.* **1969**, *244*, 3625–3634.
60. Snyder, L.R. Classification of the solvent properties of common liquids. *J. Chromatogr*. *A* **1974**, *92*, 223–230.
61. Acree, W.E.; Lang, A.S.I.D. Reichardt's Dye-Based Solvent Polarity and Abraham Solvent Parameters: Examining Correlations and Predictive Modeling. *Liquids* **2023**, *3*, 303–313.